Nuclear Inst. and Methods in Physics Research, A 1049 (2023) 168063

Contents lists available at ScienceDirect

Nuclear Inst. and Methods in Physics Research, A

journal homepage: www.elsevier.com/locate/nima

Full Length Article

Calibration of NASA's Neutron Spectrometer System (NSS) for landed measurements of hydrogen content of the lunar subsurface

P.N. Peplowski [a,*], R.C. Elphic [b], E.L. Fritzler [b], J.T. Wilson [a]

[a] Johns Hopkins Applied Physics Laboratory, Laurel MD, USA
[b] NASA Ames Research Center, Moffett Field, CA 94035, USA

ARTICLE INFO

Keywords:
Neutron spectroscopy
Lunar hydrogen
Calibration
GEANT4

ABSTRACT

NASA Ames Research Center and the Lockheed Martin Advanced Technologies Center have developed a rugged, low-resource neutron spectrometer instrument to characterize the near-surface hydrogen content of the lunar surface. This Neutron Spectrometer System (NSS) monitors local thermal and epithermal neutron rates to provide information about the depth-dependent distribution of hydrogen to depths of a few tens of cm. As of mid-2022, NSS is currently slated to fly on two NASA Commercial Lunar Payload Services (CLPS) missions; the Astrobotic Peregrine-1 lander to a near-side equatorial location, and the VIPER lunar rover to explore the polar terrain around Nobile crater. We report the results of a science calibration campaign that characterized the performance of the NSS sensors. These measurements were used to benchmark the accuracy of Geant4 radiation transport simulations that provide the energy- and angle-dependent neutron sensitivity of the NSS sensors. This information is a necessary input for converting NSS measurements of the thermal and epithermal neutron leakage flux to constraints on local hydrogen content in regions with otherwise known geochemical composition.

1. Introduction

NASA's Neutron Spectrometer System (NSS) is a compact, low-resource instrument that passively surveys the subsurface to identify locations of enhanced hydrogen content at concentrations as low as 0.5 wt% water-equivalent hydrogen (WEH). WEH reports the hydrogen concentration as if it is found entirely in water molecules. NSS measures neutrons resulting from cosmic-ray-induced spallation reactions within the lunar subsurface to estimate WEH concentrations. Orbital neutron spectroscopy is a proven technique to identify and quantify subsurface hydrogen from lunar orbit (e.g. [1,2]) at the 10+ km spatial scale. Surface-based investigations facilitate measurements at spatial scales as small as tens of cm, a three order-of-magnitude improvement over current orbital measurements. This has been demonstrated on Mars, where MSL's Dynamic Albedo if Neutrons (DAN) instrument measures neutrons produced passively, via cosmic-ray spallation, and actively, from the spacecraft-mounted pulsed-neutron generator and radioisotope power source [3].

Surface neutron emissions are a natural biproduct of interactions between near-surface materials and cosmic rays (CRs). These CRs dissociate near-surface nuclei to create a wide range of secondary particles that includes neutrons. The rate and energy-dependent shape of the surface-escaping neutron flux contains information about the composition of the planetary surface to depths of tens of centimeters. In particular, the flux of epithermal (0.2 eV to 0.1 MeV) neutrons is highly sensitive to the hydrogen content of the surface (e.g., [4,5]).

NSS measurements provide real-time indications of local hydrogen concentrations that inform decision making, such as whether or not to perform in-situ resource extraction activities. NSS has been extensively tested as part of the Phase A development of the Resource Prospector payload. Field testing of NSS, including during simulated, real-time water prospecting measurements, has been demonstrated on rovers making measurements on an alluvial fan in the Mojave desert [6] as well as the NASA Johnson Space Center rock yard facility. These activities have demonstrated the utility of neutron measurements for hydrogen prospecting, and lessons learned during these activities inform operational planning for the upcoming Peregrine-1 and VIPER Commercial Lunar Payload Services (CLPS) missions.

2. The neutron spectrometer system (NSS)

The NSS instrument (Fig. 1A) has two ^{3}He filled gas-proportional counter (GPC) sensors to characterize the local thermal (<0.3 eV) and epithermal (0.3 eV to 1 keV) neutron environment. The geometry of an NSS ^{3}He GPC sensor is shown in Fig. 1B. NSS includes a bare GPC, which is sensitive to thermal (<0.3 eV) and epithermal (0.3 eV to 1 keV) neutrons, and a GPC wrapped in a 0.63-mm-thick layer

* Corresponding author.
E-mail address: Patrick.Peplowski@jhuapl.edu (P.N. Peplowski).

https://doi.org/10.1016/j.nima.2023.168063
Received 8 September 2022; Received in revised form 12 December 2022; Accepted 18 January 2023
Available online 20 January 2023

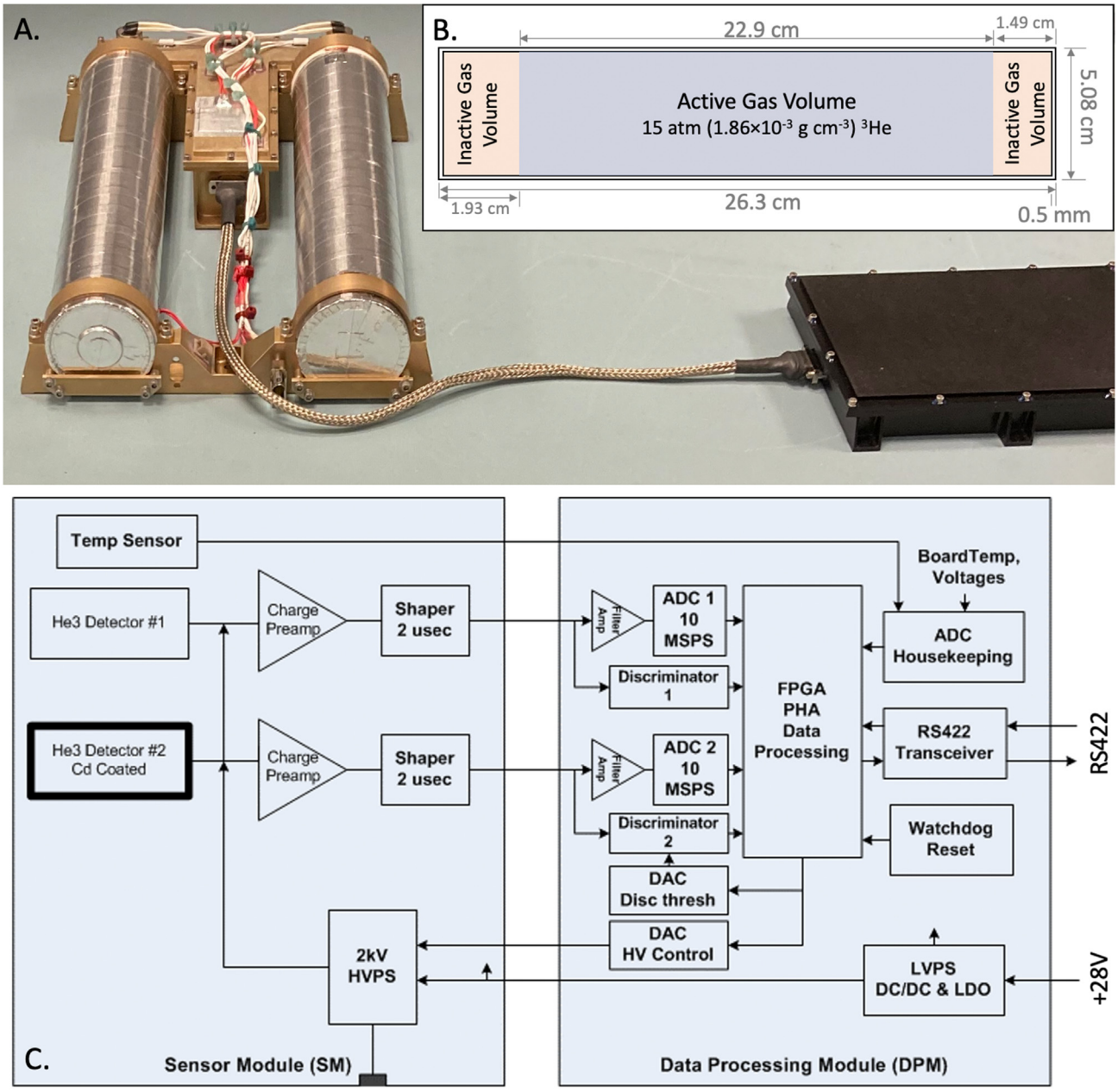

Fig. 1. A. The VIPER flight-model Neutron Spectrometer System (NSS) Sensor Module (SM) and Data Processing Module (DPM). The bare sensor is on the left, the Cd-wrapped sensor is on the right. The high-voltage supply and preamplifiers are located in the electronics module located between and above the sensors. B. A cartoon showing the dimensions of a bare NSS tube. C. A block diagram of the electronics for NSS.

of thermal-neutron-absorbing cadmium (Cd). The Cd-wrapped GPC is sensitive to epithermal neutrons only. The difference between the bare and Cd-wrapped sensor measurements yields the thermal neutron rate.

Helium-3 (^{3}He) is a common medium for neutron detection due to the high thermal-neutron-absorption cross section (5330 b) of the ^{3}He(n,p)t reaction. This reaction converts the neutral – and thus difficult to measure – neutron into two easily-measured charged particles; a proton (p) and a triton (t). The kinetic energy of these two reaction products (573 keV and 191 keV, respectively) sum to the Q-value of the ^{3}He(n,p)t reaction (764 keV). During an ideal neutron detection event, the proton and triton lose all of their kinetic energy within the ^{3}He gas, producing a signal (pulse) whose magnitude is proportional to the energy deposited (dE) in the ^{3}He gas. NSS pulse-height spectra report a histogram of all dE values, and a characteristic neutron capture peak appears at the dE value that is equal to the reaction Q-value of 764 keV. The spectra also contain features resulting from "non-ideal" events, including wall-effect events wherein a portion of the proton or triton energy is deposited in the wall of the sensor and not the gas (e.g., dE < Q). An annotated energy deposition spectrum from a bare NSS ^{3}He GPC is shown in Fig. 2.

The NSS sensors are soldered directly to the NSS sensor module electronics unit, which includes the high-voltage (HV) power supply and the preamplifiers. High-voltage values of ≥1500 V are available, in 100 V increments. The nominal operating voltage of the sensor is 1600 V. A separate electronics box, the data processing module (DPM), provides sensor control, data processing, and data handling. Mass, power, and dimensions for the NSS are listed in Table 1. Fig. 1C shows a block diagram of the NSS electronics in both the sensor module (SM) and the Data Processing Module (DPM).

The NSS DPM produces two 32-channel (1-byte-deep) spectra (one for the bare sensor, one for the Cd-wrapped sensor) at a fixed 1-second cadence. The pulse height values for each event detected in this period

Table 1
Neutron Spectrometer System (NSS) summary specifications.

Manufacturer	NASA Ames Research Center, Lockheed Martin Advanced Technologies Center
Heritage	Lunar Prospector, Resource Prospector
Sensors	^{3}He gas proportional counters (x2); see Table 2 for details
Mass (kg)	1.6
Dimensions (cm)	21.3 × 32.1 × 6.8 (sensor module) 13.9 × 18.0 × 3.0 (data processing module)
Power (W)	1.5
Count Rate Range (counts s^{-1})	≤511
Sensitivity (Effective Area; cm^2)	80 cm^{-2} (@ 1eV)
Field-of-view	4π steradian
Survival Temperature Range (°C)	−40 to 60 (sensor module) −40 to 60 (data processing module)
Operating Temperature Range (°C)	−30 to 40 (sensor module) −30 to 50 (data processing module)
Operating Voltage Range (VDC)	28 ± 6
Interface	RS-422
Bits/sample	712
Sampling Rate (s^{-1})	1

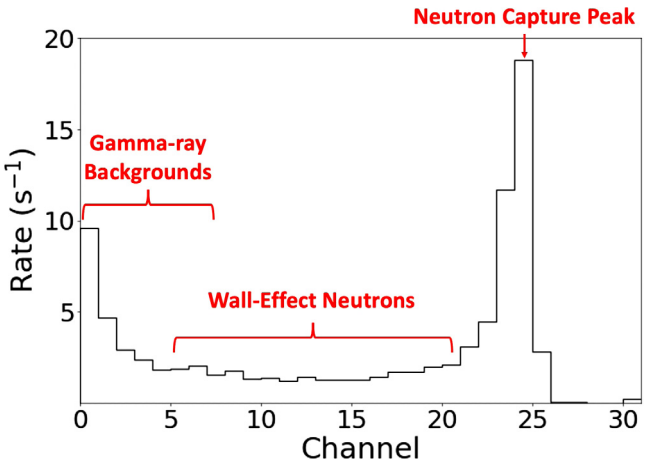

Fig. 2. Annotated energy deposition spectrum from a bare NSS sensor, highlighting the neutron capture peak (dE = Q = 764 keV), the wall effect features, and low-energy gamma-ray backgrounds.

are recorded in the spectrum, separately for each sensor. The short measurement cadence facilitates spatially resolved measurements for rover-mounted NSS implementations (e.g. VIPER), as the spectra can be summed as informed by the details of the rover traverse. The DPM has six preset, commandable lower-level thresholds that exclude low-energy (low-channel) noise from the data products. The gain of the spectra are fixed, therefore the location of the 764-keV neutron capture peak is set by the bias voltage alone. A sample NSS spectrum is shown in Fig. 2 for 1600 V bias and a threshold value of zero (no threshold).

Quantifying hydrogen abundances from NSS measurements requires spectral analysis, knowledge of the sensor response, and radiation transport simulations. First, the neutron rate must be derived from the energy deposition spectra (e.g. Fig. 2), including corrections for non-neutron sources of events such as detector noise and dE signals originating from gamma rays and protons. These particles are abundant on the lunar surface. Corrections to the detector live time and temperature-dependent gain may also be required. Second, the energy- and angle-dependent neutron detection efficiency of each detector must be precisely known in order to convert neutron counting rates (e.g. counts s^{-1}) to the local neutron flux (neutrons cm^{-2} s^{-1}), a necessary step for deriving hydrogen concentrations from NSS measurements. Finally, the measured neutron fluxes are compared to predictions from radiation transport simulations to constrain the elemental composition of the lunar soil beneath the sensor, including its hydrogen content. These simulations also incorporate estimates of local background signals resulting from neutron production and scattering with the systems that host NSS, whether lander or rover.

3. NSS calibration campaign

3.1. Overview

We report the results of a calibration campaign designed to quantify the performance of the NSS. The calibration efforts involved three phases. The first phase (Section 3.2) was a set of measurements on a bare tube identical to those in the NSS units, and was executed to characterize the intrinsic performance of the sensors and to provide a performance benchmark for radiation transport simulations. This includes the response of the sensor to neutrons and gamma rays, characterization of detector noise, and measurements of the active area of the sensor. The second phase of the calibration (Section 3.3) characterized the performance of the NSS in the presence of radioactive sources, including a neutron-moderating pile designed to produce lunar-like neutron spectra. These activities were performed with the VIPER flight-model NSS sensor. Phase three of the calibration (Section 3.4) was thermal-vacuum testing of the engineering test unit (ETU; #2) NSS, which validated operation in space-flight pressure and thermal environments, and provided data necessary to characterize the performance of the NSS as a function of temperature.

3.2. NSS ^{3}He Sensor Calibration

The intrinsic performance of a bare NSS ^{3}He GPC was characterized at the Johns Hopkins Applied Physics Laboratory (APL) using laboratory-grade electronics and radiation sources in the configuration shown in Fig. 3. During all testing, the sensor was placed within a 1-cm-thick polyethylene neutron energy moderator, and its single electrical connection was attached to a Kromek eV-550 preamplifier. Detector high-voltage was supplied by a CAEN high-voltage power supply, and data analysis was performed with an Amptek 8000A multi-channel analyzer.

The sensor performance was characterized versus bias voltage using neutron (^{252}Cf, AmBe) and gamma-ray (^{228}Th) sources. Fig. 4 compares sensor measurements with the commercial setup to those provided by the NSS DPM. The sensor characterization measurements reported here oversample the pulse-height spectra, providing a 512-channel spectrum as compared to the 32-channel NSS spectra. This oversampling provides an opportunity to study the sensor response in detail. Fig. 5 plots measurements with the neutron and gamma-ray sources, at the nominal operating voltage of 1600 V. The data highlight several features of the energy-deposition spectra, including the relative locations of the

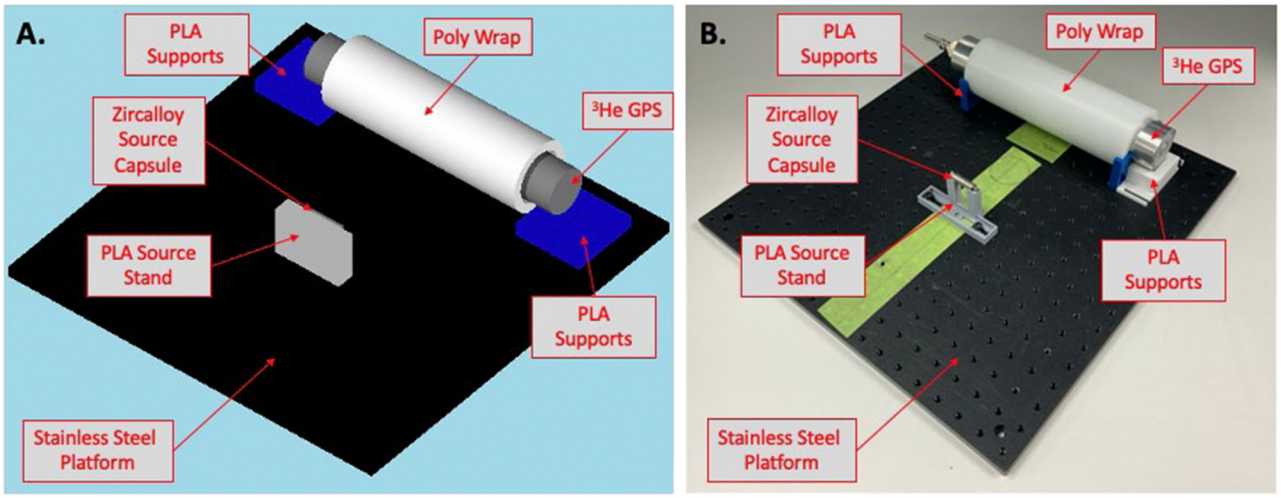

Fig. 3. The NSS sensor benchmarking setup, showing a bare ^{3}He gas proportional counter sensor, located in a 1-cm-thick polyethene neutron moderator. Low-mass, 3-D-printed stands support the sensor, polyethylene, and ^{252}Cf source. A. Geometry as included using the radiation transport simulation toolkit Geant4. B. An image of setup.

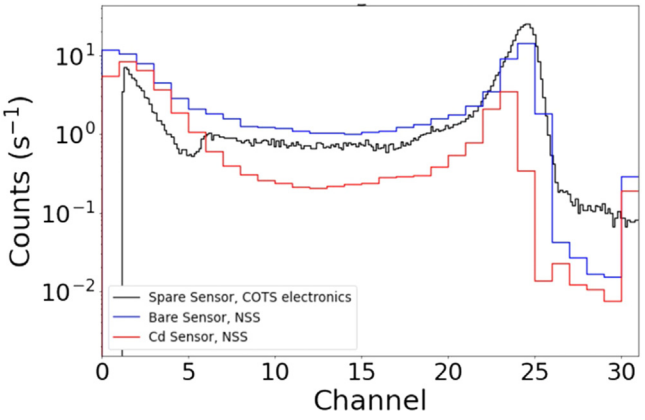

Fig. 4. A comparison of the NSS spare sensor measurements with laboratory-grade electronics to the flight-model NSS measurements. The x-scale of the 512-channel spare-sensor measurements were matched to the NSS bare sensor scale. Note the ~1-channel difference in gain for the neutron capture peak between the NSS bare- and Cd-wrapped sensors.

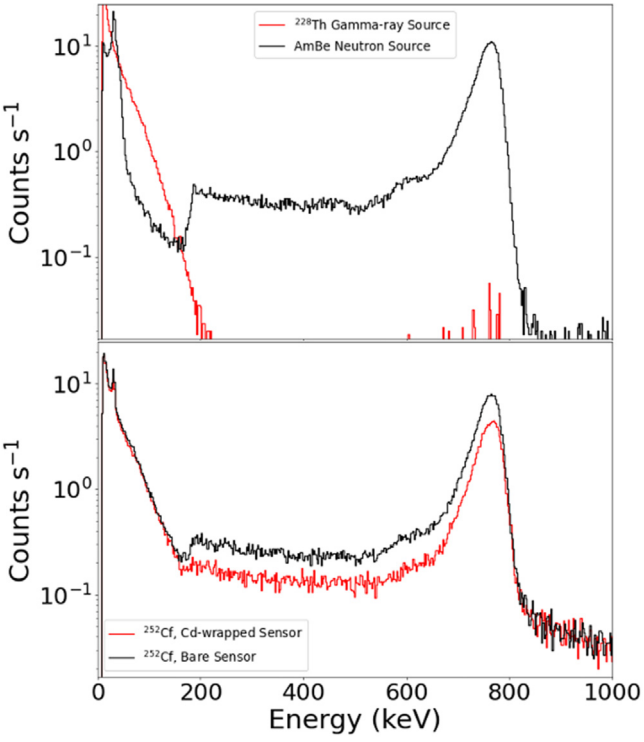

Fig. 5. (Top) Pulse height spectra from the NSS spare sensor (with laboratory-grade electronics), showing measurements from a gamma-ray source (red) and a neutron source (black). A room-background spectrum was subtracted to create these spectra. (Bottom) Pulse height spectra from the NSS spare sensor, with (red) and without (black) a 0.5-mm-thick Cd foil wrap. These measurements were collected with a ^{252}Cf source, which also emits gamma-rays that are visible in the spectra. Note the presence of the no-gain peak around 35 keV.

gamma-ray and neutron signals, as well as the effect of adding a Cd neutron-absorbing wrap.

Application of high-voltage bias to a ^{3}He GPC produces an electrostatic potential within the active volume of the sensor (Fig. 1b) that results in multiplication of ionization electrons, resulting in increased signal gain. As amplification occurs relative to electronics noise, gas gain facilitates clean analysis of the neutron spectrum by amplifying the signal but not the noise. Fig. 6 shows the gas gain of the NSS GPC versus bias voltage, measured as the position of the neutron capture peak relative to the position of the no-gain peak, which is due to neutron capture events in the non-biased (in-active; Fig. 1B) region of the sensor. As seen in Fig. 6, more bias voltage results in more gas gain. Increased bias also causes spectral degradation as manifested as decreased resolution (increased width of the neutron capture peak). This phenomenon is shown in Fig. 7, which plots the full-width at half maximum (FWHM) of the neutron capture peak versus bias voltage. For the NSS nominal operating voltage of 1600 V, the intrinsic gas gain within the sensor is 17, and our commercial electronics yield a FWHM of ~5.4%. Note that because of the non-Gaussian shape of the neutron capture peak, the FWHM is calculated numerically by finding the pulse-height channels whose count rate is half the maximum count rate in the peak, and calculating the width from the distance between those channels. This technique yields the true FWHM of the peak, including contributions from the tail on the low-energy side.

Fig. 8 details the counting rate of the sensor, in the presence of a ^{252}Cf neutron source, as a function of bias voltage. The data show that the counting rate is stable versus bias voltage for our operating range of interest. Confirmation of stable neutron detection efficiency in our operating range of interest removes a potential systematic uncertainty in the interpretation of NSS measurements (See Section 5).

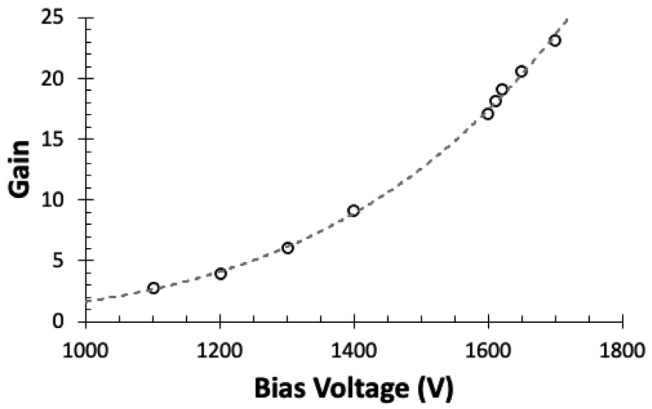

Fig. 6. The gain of the NSS spare sensor plotted as a function of bias voltage.

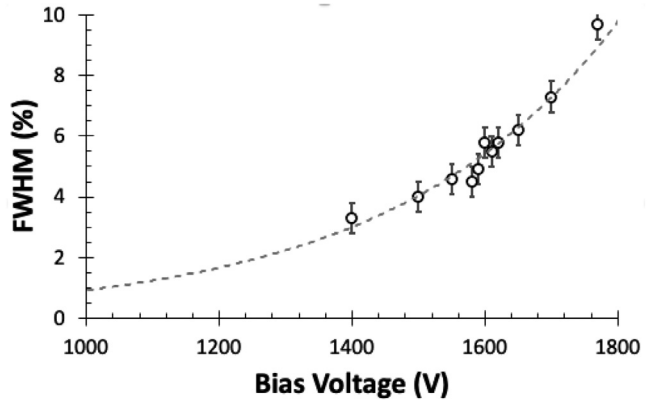

Fig. 7. The neutron-capture peak width of the NSS spare sensor plotted as a function of bias voltage.

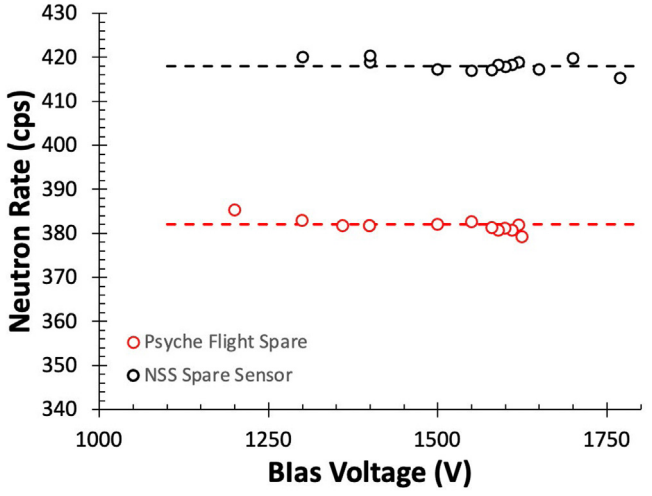

Fig. 8. Neutron rates from a ^{252}Cf neutron source, at a fixed position 20 cm from the sensor, as a function of high-voltage bias. The 1-standard-deviation statistical uncertainties of these measurements are smaller than the size of the data points.

The measurements detailed above were repeated with the same experimental setup for a ^{3}He GPC sensor from the NASA Psyche Gamma-Ray and Neutron Spectrometer (GRNS). The Psyche sensor measurements were performed for two reasons. First, the Psyche sensor is similar to the LP NS sensors (see Table 2), and LP NS is the standard by which many prior NSS sensitivity calculations have been compared. Fig. 8 shows that the NSS sensor has a higher neutron

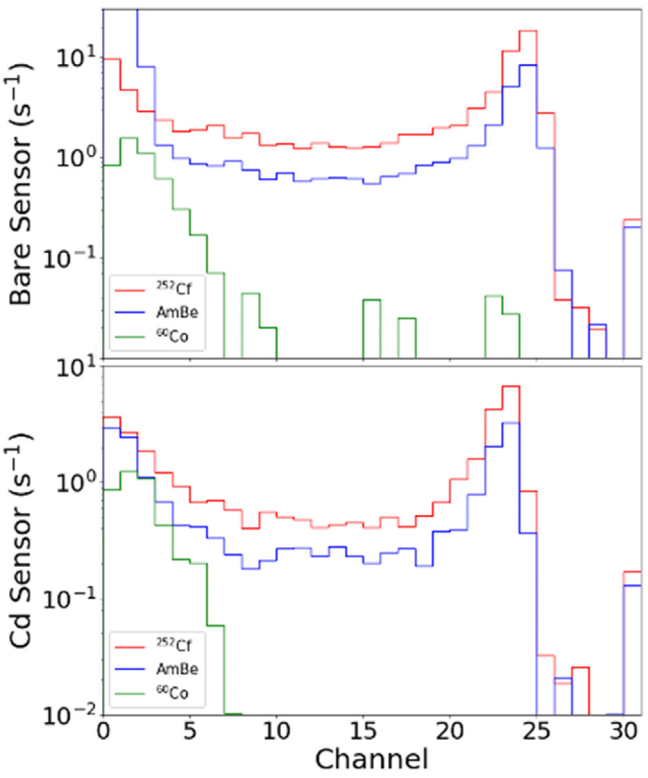

Fig. 9. VIPER flight-model NSS measurements for neutrons (^{252}Cf and AmBe sources) and gamma rays (^{60}Co). Room background spectra were subtracted from the measurements.

detection efficiency than the Psyche sensor. The increased sensitivity is due to the higher gas pressure of the sensor (15 atm vs. 10 atm for Psyche). Accordingly, the NSS sensitivity is likewise higher than the 10-atm-pressure LP NS. Second, the Psyche sensor underwent a detailed calibration campaign at the Nation Institute for Standards and Technology (NIST) Center for Neutron Research, and the resulting measurements informed a high-fidelity Geant4 radiation transport simulations of that sensor [7]. Cross calibration of the NSS and Psyche sensors provides a tie point for developing the NSS simulations via a NIST-traceable calibrated GPC (see Section 4).

3.3. *VIPER flight model NSS sensor calibration*

3.3.1. *Spectral performance*

The performance of the flight-model VIPER NSS unit was also characterized at APL. For these measurements, high-voltage bias and signal processing were performed by the NSS DPM. The measurements are shown in Fig. 9, and they highlight the differences between neutron- and gamma-ray induced signals in the NSS spectra. Specifically, we see that gamma-ray-induced signals in the ^{3}He gas are predominately located in channels <7, and decrease with increasing channel number. This gives an early indication of favorable threshold channel values.

These spectra also highlight an important feature for the VIPER NSS — at identical high-voltage bias settings of 1600 V (commanded, 1584 V reported by the DPM), the neutron capture peak centroids differ by ~1 channel (3%). This difference may be due to mismatched electronics components in the signal processing chains for the two sensors. If so, the position of each peak centroid in each NSS unit will vary and the flight-model VIPER NSS tested here may not be representative of other NSS units (e.g. Peregrine -1).

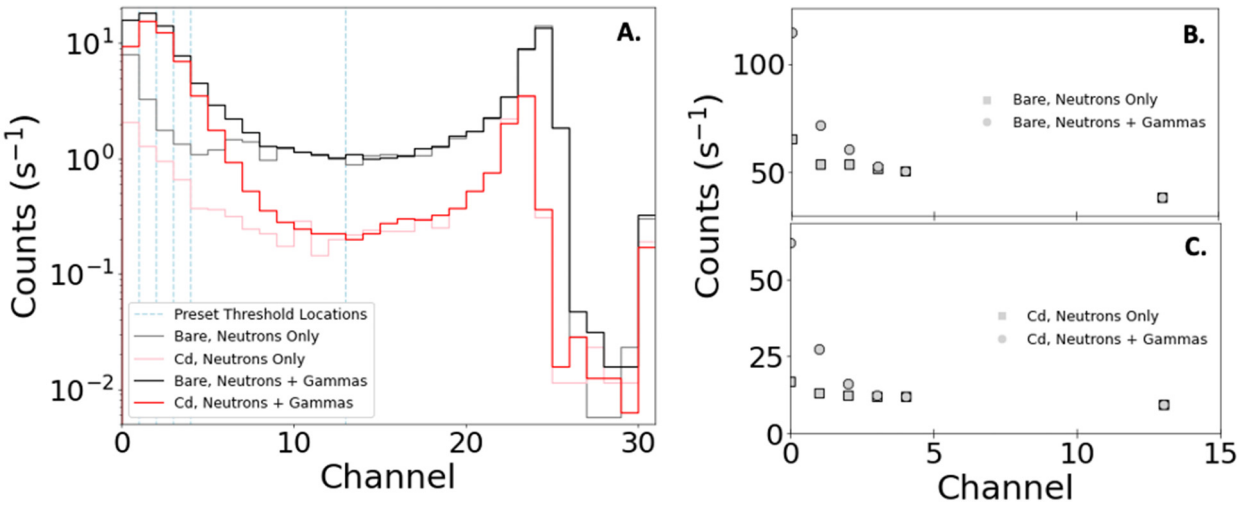

Fig. 10. A. Sample NSS spectra, with and without a high-intensity gamma-ray source nearby, for both NSS sensors. Available thresholds are shown as vertical dashed lines. B. Total count rate in the bare sensor (all events in spectrum) versus threshold value, for neutrons only and neutrons plus gamma rays. C. Same as panel B., for the Cd-wrapped sensor.

Table 2
Threshold name and channel value.

Threshold name	Channel value
"31 keV"	0
"62 keV"	1
"94 keV"	2
"124 keV"	3
"165 keV"	4
"441 keV"	13

3.3.2. Pulse processing thresholds

As shown in Figs. 2, 5 and 9, the low-channel portion of the spectrum is dominated by gamma rays, not neutrons. In space, cosmic-ray protons will also contribute to the low-channel counts. Application of an event threshold provides a mechanism to filter out these background signals. The threshold is applied on an event-by-event basis to signals that are processed by the DPM and included in the pulse-height spectrum. The commanded threshold is used in two ways: (1) it sets the analog discriminator threshold for the scalar count accumulation process, and (2) the FPGA is configured to reject digital pulses that fall below the threshold value.

The flight software provides six pulse-amplitude threshold options. These options, which are labeled by their approximate energy value, correspond to specific channel values as listed in Table 3. It is important to note that the energy values are approximate, and are only valid when the sensor is biased to 1600 V. Additionally, because the gain of the bare and Cd-wrapped sensors differ by ~1 channel (see Fig. 9), a single threshold value does not have an equivalent effect on the two pulse-height spectra. Finally, note that the gain of both sensors is temperature dependent (see Section 3.4), and thus the relative fraction of background versus signal events above and below the threshold may vary with temperature (see Fig. 10).

The effect of each threshold on reported counting rates was explored using a series of measurements aimed at separating neutron and gamma-ray induced signals. For the first set of measurements, a moderated AmBe source was placed near the NSS sensor module. A lead brick was placed between the source and the sensor to reduce the gamma-ray flux at the sensor, making this a neutron-dominated environment. The NSS counting rate was sampled versus threshold value in this setup. The measurement was then repeated, with a high-activity ^{228}Th gamma-ray source nearby. When the rates from the two types of measurements are identical, the "background" gamma-ray component introduced by the ^{228}Th source has been successfully removed. At 1600 V bias, this condition is achieved with the channel 3 ("124 keV") threshold for both the bare and Cd-wrapped sensors. For lower thresholds, gamma-ray events are included in total rates, as demonstrated by the higher rates with the gamma-ray source is present. For higher thresholds, gamma rays do not contribute, however the highest threshold (channel 13) removes some neutron signal-of-interest, as exhibited by the lower rate for this value. Section 5 discusses considerations for threshold selection based on these measurements and other operational considerations.

3.3.3. Lunar neutron flux benchmark

Cosmic-ray protons do not reach Earth's surface, so an alternative means of generating planetary-like neutron spectra is required to perform flight-like measurements in a laboratory setting. A neutron-moderating pile (NMP) of reactor-grade graphite, located at APL and inspired by the mini-pile of Feldman et al. [8], was designed to provide a unique tool for producing planetary-like spectra from laboratory neutron sources. The core of the NMP is a reconfigurable stack of blocks made from 900 lbs. of nuclear-grade graphite. Nuclear-grade graphite is highly refined to remove impurities that otherwise modify the neutron spectrum, particularly neutron-absorbing boron. As a historical aside, the graphite for the NMP was supplied by GrafTech, the same company that supplied graphite for Fermi's 1942 Chicago pile CP-1, the world's first artificial nuclear reactor. The graphite they supplied for the NMP was their final supply of reactor-grade material. Thus, the VIPER calibration is the culmination of a story that began at the dawn of the nuclear age.

The NMP graphite stack area is 24" × 24", and the height is 20" (Fig. 11b). A hole is located in one of the bricks, which enables a neutron source to be placed in the center (length, width) of the pile. An Americium–Beryllium (AmBe) source provides the initial neutron source for the NMP. AmBe sources produce neutrons via an alpha particle (α) capture reaction that is initiated by the α-decay of ^{241}Am ($t_{1/2}$ = 432.6 yr). That reaction series is:

$$^{241}\mathrm{Am} \rightarrow {}^{237}\mathrm{Np}(t_{1/2} = 2.1 \times 10^{6}\mathrm{yr}) + \alpha$$
$$^{9}\mathrm{Be} + \alpha \rightarrow {}^{12}\mathrm{C} + \mathrm{n} + \gamma.$$

Our simulations of the NMP neutron flux begin by assuming an AmBe neutron flux as reported by Marsh et al. [9]. Amongst typical laboratory neutron sources, AmBe is the best choice for the NMP because of its long half life, its neutron energy range that extends to higher energies than ^{252}Cf, and because its only non-neutron background, the 4.438-MeV gamma ray emissions, will be present regardless of the neutron

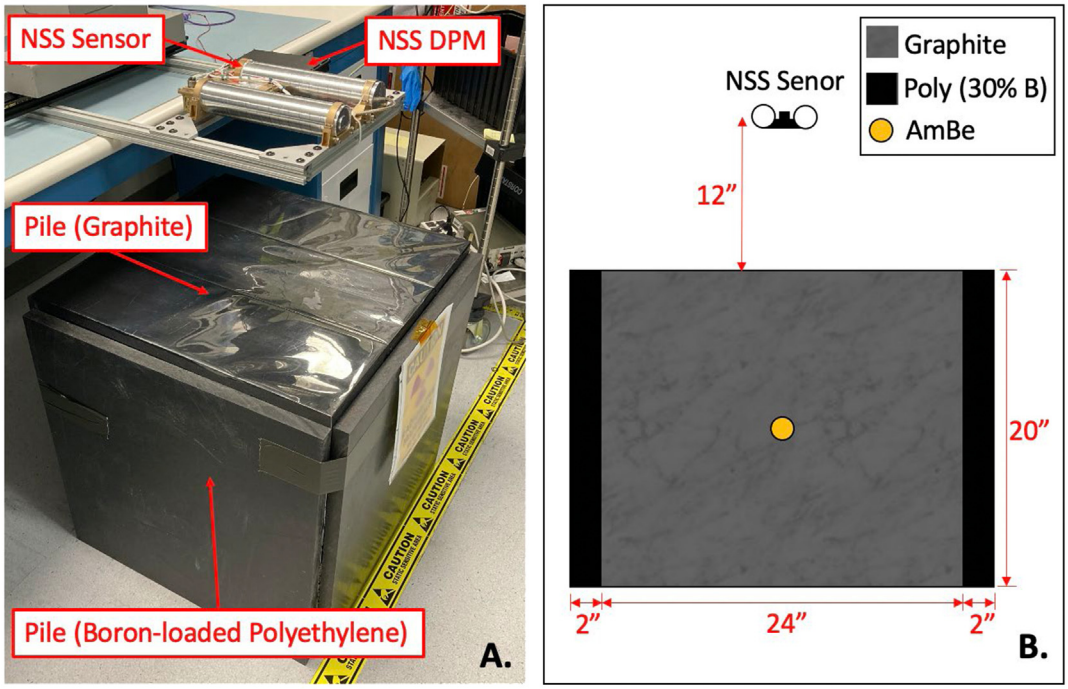

Fig. 11. A. Annotated photograph of the NSS sensor module (SM) and data processing module (DPM) above the neutron-moderating graphite pile. B. A cartoon of sensor above pile, with the dimensions. Here “Poly” is polyethylene, and “AmBe” is the location of the ^{241} Americium–Beryllium neutron source.

source due to neutron inelastic scattering interactions with ^{12}C in the graphite.

The pile is surrounded on all sides, but not the top or bottom, by 1”-thick sheets of borated high-density polyethylene. The 30% boron content of the sheets absorbs >75% of all neutrons emerging from the sides of the NMP, significantly reducing the room-background neutron flux and thus scattered-neutron backgrounds. The top of the NMP does not have a permanent polyethylene cover. Instead, polyethylene sheets of varying thicknesses (1/8” to 2”) and boron content (0, 5%, and 30% natural boron) are available to be placed on the top of the pile to vary the spectral shape of the neutron flux emitted at the upper (sample) surface.

Geant4 simulations of the NMP, with varying top-sheet configurations, were performed to identify a set of configurations that would yield lunar-like neutron spectra for NSS calibration. See Section 4 for details. A separate set of Geant4 simulations explored neutron spectral shapes for CR-induced neutron production on different lunar soils (ferroan anorthosite versus mare basalts) and hydrogen concentrations (0 to 2500 ppm). Nine NMP configurations were ultimately selected (see Table 4) to provide lunar-like spectra. Fig. 12 compares simulated lunar neutron spectral shapes to those at the top of the neutron pile for the nine configurations listed in Table 4. The simulations indicate that the selected pile configurations reproduce the gross neutron energy-dependent flux features that are expected for measurements made at the lunar surface.

The VIPER flight-model NSS instrument was positioned directly over the NMP for the lunar-like spectral measurements (Fig. 11a). The center of the NSS sensors were 12” above the top of the NMP, as measured prior to the addition of the polyethylene sheets (e.g. Configuration #1; Table 4). The NSS-measured count rate versus time for each configuration, along with sample spectra, are shown in Fig. 13. These measurements provide an indication of typical NSS measurements. For example, moving from configuration #1 to #4 is analogous to moving from hydrogen-poor to hydrogen-rich (>100s of ppm H) materials. As seen in Fig. 13, this corresponds to a decrease in the epithermal neutron rate as measured with the Cd-wrapped sensor, with additional variability in the bare sensor, which samples thermal and epithermal neutrons.

Table 3
Thickness and boron content of the top polyethylene sheets used during neutron-moderating pile calibration measurements.

Configuration	Thickness (in)	Boron (%)
1	n/a	n/a
2	0.5	0
3	1.0	0
4	1.5	0
5	2.0	5
6	1/8	5
7	1/4	5
8	1/2	5
9	1	5

These measurements provide a crucial benchmark for assessing the accuracy of radiation transport simulations of NSS performance in a lunar-like environment, as discussed in Section 4.

3.4. Environmental testing

NSS thermal-vacuum testing was performed with an environmental test unit (ETU; #2) on 9 September 2019. The entire NSS (sensor and data processing module) was placed in the vacuum chamber at NASA ARC Engineering Evaluation Laboratory, evacuated to $<10^{-5}$ torr, and cycled from −38 °C to +62 °C. A low-activity ^{252}Cf neutron source was placed outside of the vacuum chamber during NSS operation, facilitating monitoring of the pulse-height spectra throughout the test.

Summed spectra, collected using measurements acquired at two temperature extremes (>58 °C; “hot”) and (<−35 °C; “cold”), were used to constrain the impact of temperature on the science data products. Because the sensor module and data processing module temperatures varied together, we cannot isolate separate effects and instead examined when the entire system was hot and cold. The summed spectra, shown in Fig. 14, show a gain shift of ~1 channel per over this ~95 °C temperature swing for the bare sensor, and ~2 channels for the Cd-wrapped sensor. In-flight NSS spectral gain versus instrument temperature should be monitored and, if comparable temperature swings are seen in flight, then NSS data should be gain corrected using

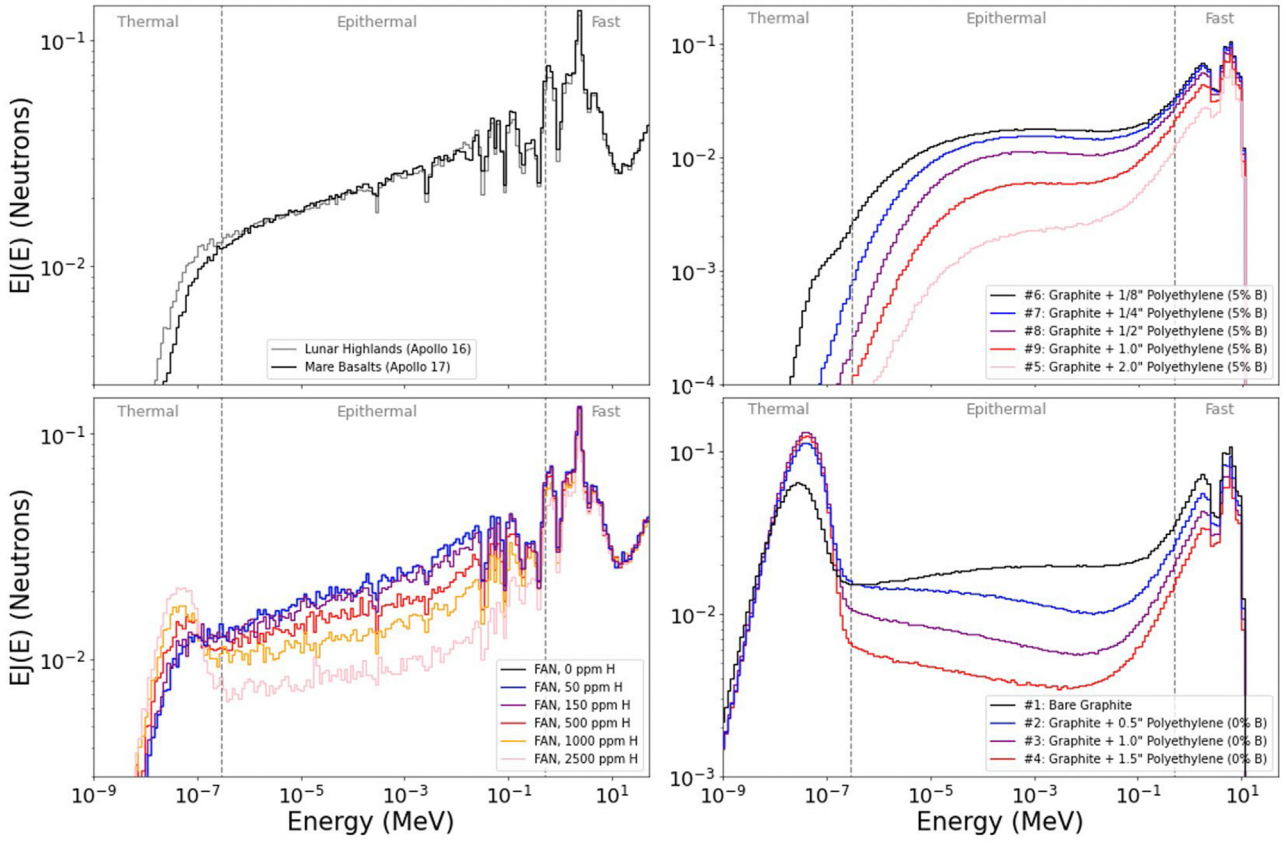

Fig. 12. Geant4-simulated neutron emission spectra for simulations of cosmic-ray-induced neutron production on the Moon (right) and from the APL neutron pile with an AmBe source (left).

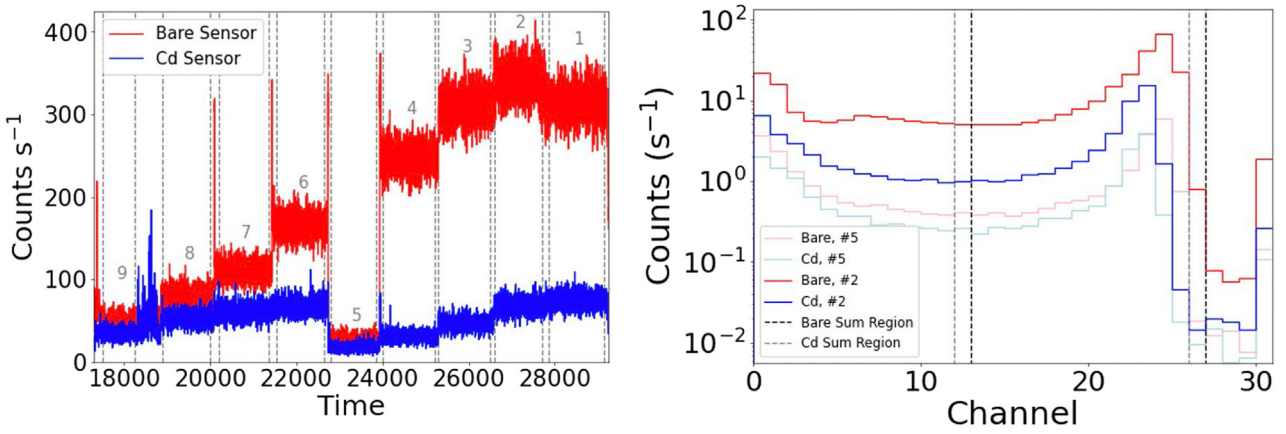

Fig. 13. (Left) Time-series data of the bare- and Cd-covered sensors for each pile configuration (numbered; see Fig. 15 legend). (Right) Sample spectra from two of the pile configurations, with dashed lines indicating the summing region used to derive the neutron capture peak rates.

the sensor temperature telemetry during on-the-ground post processing of the spectra. This correction should be performed prior to spectral summing to preserve energy resolution and avoid changing the spectra relative to fixed-channel summing intervals.

4. Simulated NSS response

4.1. Overview

NSS measures pulse height spectra that are used to derive counting rates in the bare and Cd-wrapped neutron sensors. Analysis of these spectra can yield the local thermal and epithermal neutron fluxes. Converting these fluxes to information about subsurface hydrogen content requires iterative comparison between measured and simulated neutron fluxes. The simulations include detector response information, specifically how likely a neutron is to produce a signal in the sensors as a function of its energy and sensor-incidence angle. The calibration data detailed in Section 3 provides experimental benchmarks to assess the accuracy of this portion of the radiation transport simulations.

Our radiation transport simulations were performed using Geant4, version 10.07.1. Our code was derived from the example AnaEx01. We modified the DetectorConstruction file to add the ^{3}He GPCs, using the geometry shown in Fig. 1. We also modified the code to utilize the standard Geant4 Physics Lists, in our case using the “Shielding” list that was developed for use in space radiation environments. We

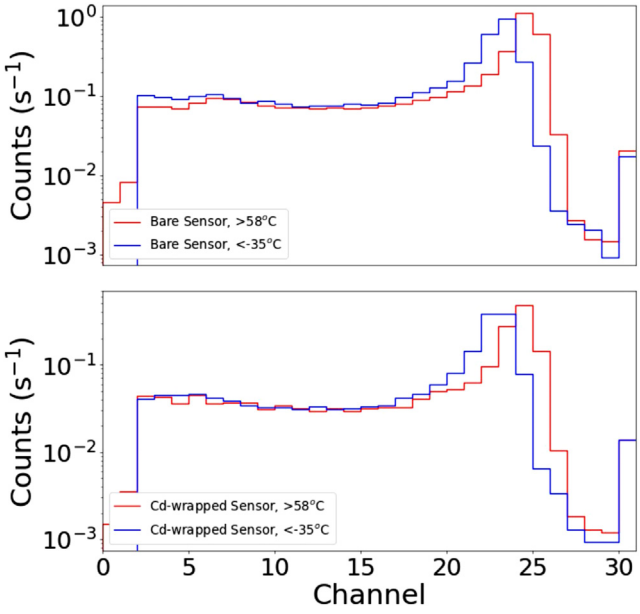

Fig. 14. Summed pulse-height spectra, collected during thermal-vacuum (TVAC) testing of the NSS Environmental Test Unit (ETU) #2. (Top) Bare-sensor spectra, summed using all data collected while the sensor module is >58 °C (red, "hot") and <−35 °C (blue, "cold"). (Bottom) Cd-wrapped-sensor spectra, summed using all data collected while the sensor module is >58 °C (red, "hot") and <−35 °C (blue, "cold").

also modified the code to allow for sources to be defined using the built-in GeneralParticleSource framework. Finally, we modified the EventAction file to record only events that deposit energy in a detector volume, in this case the "active gas volumes" shown in Fig. 1.

Our Geant4 startup file calls the G4NDL 4.6 neutron cross section library. Per the recommendations found in the Geant4 Application Developers Guide (release 10.4), which recommends additional environmental variable settings for applications seeking accurate neutron physics simulations, we set the following options in the startup file:

export G4NEUTRONHP_NEGLECT_DOPPLER=1
export G4NEUTRONHP_DO_NOT_ADJUST_FINAL_STATE=1
export G4NEUTRONHP_SKIP_MISSING_ISOTOPES=1
export AllowForHeavyElements=1

These options improve neutron-induced reaction accuracy and/or lower computational time for the simulations.

4.2. ^{3}He GPC Simulation Benchmarking

The sensor plus commercial electronics measurements detailed in Section 3.2 provide a high-fidelity benchmark for characterizing the accuracy of the ^{3}He GPC sensor-response portion of the Geant4 simulations. Fig. 3 details the geometry of the sensor and support structures for those measurements, including as simulated with Geant4. For those measurements, the sensor and electronics (Fig. 3) were placed on a low-mass test stand in the middle of the laboratory, with the goal of reducing background signals from room-scattered neutrons. As a consequence, we did not include the room or any interior materials in the simulations. The simulations do include the neutron sensor (size, active length, ^{3}He fill pressure, etc.; see Table 2), the 1.2-cm-thick hollow-cylinder polyethylene neutron moderator, the 0.5-mm-thick Cd wrap (when present), and the Zircaloy-alloy ^{252}Cf source encapsulation. All objects in the simulation have masses that are within a few percent of their measured masses. Geant4 materials with thermal neutron scattering (TS) properties are specified where available, which includes the use of "TS_H_of_Polyethylene" for the H in the moderator. Isotopically pure ^{3}He gas is specified for the sensor gas.

Table 4
Dimensions and gas pressure for NSS neutron sensor, and for comparison those of the Psyche and Lunar Prospector neutron instruments.

Quantity	Sensor		
	NSS	Psyche[b]	Lunar prospector[c]
Housing Material	Stainless Steel	Aluminum	Stainless Steel
Housing Thickness (mm)	0.9	1.4	0.6[d]
^{3}He fill Pressure (atm)	15	10	10
Outer Diameter (cm)	5.09	5.05	5.82
Active Diameter (cm)	4.91	4.77	5.7
Total Length (cm)	24.1	30.6	29
Active Length[a] (cm)	20.0	25.4	20
Cd-wrap thickness (mm)	0.63	0.5	0.63

[a]As quoted by the manufacturer, the true active length can vary (e.g. [7]).
[b]As provided by the manufacturer and detailed in Peplowski et al. [7].
[c]From Feldman et al. [5].
[d]From Lawrence et al. [10].

The ^{252}Cf source is treated as a point source, at the center of the source encapsulation, and is located exactly 20 cm from the center of the sensor. Following Radev and McLean [11], we specified the neutron-energy-dependent flux of neutrons $N_n(E_n)$ from the ^{252}Cf source using a Watt spectrum:

$$N_n\left(E_n\right) = e^{-E_n/a} sinh(\sqrt{bE_n}) \quad (1)$$

where N_n is the number of neutrons per unit energy, E_n is the neutron energy, and a and b are tuned for ^{252}Cf and have values of 1.18 and 1.03419, respectively. The ^{252}Cf neutron spectrum peaks at 2.13 MeV, with 90% of the neutrons having energies less than 4.4 MeV.

The simulations were performed four times, twice for each sensor (NSS, Psyche), with and without the Cd wrap. One-hundred million histories were run for each scenario. All histories resulting in particles that lose energy within the detector active volume were tallied and stored in a histogram that is directly comparable to the pulse-height measurements. The same summing region (wall effect + neutron capture events) is used for the measurements and simulations. The simulation-versus-measured counting rates are compared in Fig. 16. There are no arbitrary normalizations applied to this comparison. All four of the benchmarks have a simulation-to-measurement match of 6% or better (dashed lines; Fig. 15). We track this as a systematic uncertainty in the accuracy of our simulated detector response (see Section 5). The simulation-to-measurement agreement for the NSS sensors can be improved slightly by reducing the active area of the NSS sensor (e.g. Fig. 1b) by 1.5%. We do not adopt this normalization, however given previous work showing a loss of active area in GPC sensors due to dead-region edge effects [7], we track this as a possible systematic uncertainty in our knowledge of the active area of the sensor (see Section 5).

4.3. Lunar-like measurement simulation benchmarking

The NMP-neutron-source measurements detailed in Section 3.3.3 provide data that can be used to benchmark the accuracy of the Geant4 radiation transport simulations, this time with lunar-like neutron spectra. For those simulations, the Geant4 code was modified to include both NSS sensors, with and without the Cd wrap, in a geometry identical to that of the NSS sensor (see Fig. 1). The neutron pile was simulated as a solid block of graphite, and the Geant4 material "TS_C_of_Graphite" was used to ensure that the thermal neutron scattering within the pile was accurate for low-energy neutrons.

As was the case for single-sensor measurements (Section 4.2), our GEANT4 simulations of the NMP measurements did not include the room. That simulation geometry was restricted to the NMP and NSS sensor only. Because the simulations do not include room return, whereas the measurements do, the simulations are expected to underestimate the measured counting rates (see Fig. 16).

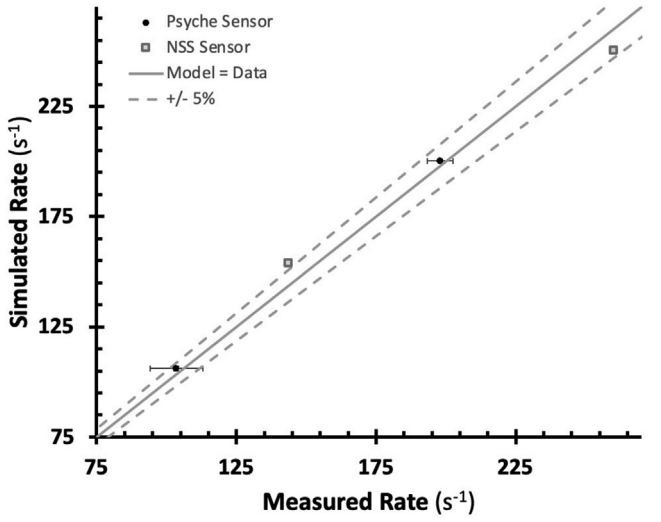

Fig. 15. Benchmark of the Geant4 simulations, showing simulated versus measured rates for the spare sensor data (see Fig. 2 for measurement geometry). For both the Psyche and NSS sensors, bare- and Cd-wrapped, the simulations match the measurements to within 6%. The error bars on the simulated measurements are smaller than the data points.

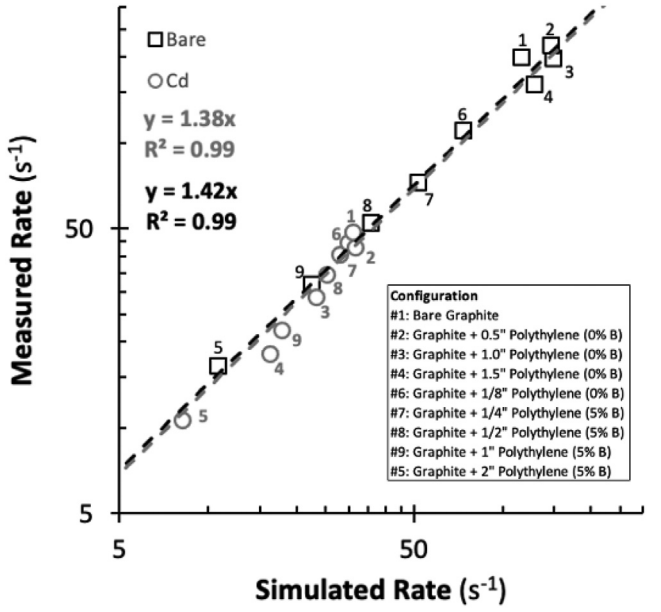

Fig. 16. Measured vs. simulated neutron capture rates, for both the bare- and Cd-covered sensors, for each neutron pile configuration (See legend). Linear fits demonstrate that the scatted room background contribution to each measurement is ~40% (see Section 3.4), as well as the strong correlation between the measurements and simulations ($R^2 = 0.99$).

We leveraged the fact that the geometry of the experiment is fixed to develop an analytical model of the room-scattering background, based on the assumption that it scales linearly with the total neutron flux from the NMP. The model relates the measured counting rate R to the simulated rate S as:

$$R = (1 + F_S)S + B \tag{2}$$

where F_S is the fraction of neutrons reaching the sensor following scattering in the room, and B is the non-NMP rate of events from natural radioactivity in the room. Measurements of room background with no sources present indicated that B is close to zero, therefore we neglect that term.

Table 5
Systematic Uncertainties in the Analysis of NSS measurements.

Quantity	Value	Justification
Accuracy of the Geant4 simulations	≤6%	see Fig. 15
Uncertainty in NSS sensor active area	~1.5%	See Section 4.2
Efficiency at unstable/uncertain bias voltage	<1%	See Fig. 8
Total	**≤6.3%**	

Fitting the measured rates R against the simulated rates S, separately for the bare and Cd-wrapped sensor measurements, yields $F_S = 0.38$ and 0.42 for the Cd-wrapped and bare sensor measurements, respectively. See Fig. 16. The correlation coefficients between the measured and simulated rates are high ($R^2 = 0.99$) for both sensors. With the background estimates included, we find that over half of the simulations are within 5% of the simulated detector counting rate, and 95% are within 20%. This result is generally consistent with our adopted uncertainty for the Geant4 radiation transport simulations (≤6%). It is important to note that there is an additional systematic uncertainty here, the accuracy of the simulated pile neutron spectra, that is not relevant to NSS measurements.

4.4. NSS sensor simulation benchmarking

Our calibration measurements and simulation benchmarking activities facilitate a stack up of the total systematic uncertainties associated with our knowledge of the response of the NSS sensors and our ability to accurately simulate it. The uncertainties are listed in Table 5, and when added in quadrature yield a total systematic uncertainty of ≤6.3%. With this information, we are confident in our ability to extend the Geant4 simulations to predict the neutron-energy and sensor-incident-angle detection efficiency of the NSS sensors.

The Geant4 simulations direct neutrons toward the NSS sensors in a plane wave of dimensions 30 cm × 30 cm. The area is significantly larger than the sensors, and the neutron fluence is 1111.1 n cm^{-2} per simulation. A separate simulation was carried out for each neutron energy and angle. The coordinate system for the simulations is defined such that, at 0° incidence angle, the momentum vector of the neutrons is perpendicular to the long axis of the sensor. The projected active area A_P of each NSS sensor in the z–y plane is calculated as a function of angle as:

$$A_P = 2rH\sin\theta + \pi r^2\cos\theta \tag{3}$$

where r is the radius of the active gas volume (5.52 cm; the sensor diameter minus the wall thickness), H is the length of the active volume (20 cm), and θ is the incidence angle.

The Geant4 code simulated 1,000,000 neutron histories at each incidence angle. For each simulation, Geant4 produces a list of all energy deposition (dE) events in the sensor. This event-by-event list was converted to a histogram of dE values from 0 to 1000 keV, and all neutron events (wall effect and neutron capture peak) are summed. The efficiency $\varepsilon(E_n, \theta)$, defined as the probability that a neutron will be detected by the NSS, is then calculated as:

$$\varepsilon(E_n, \theta) = \frac{N(E_n, \theta)}{\Phi_n A_p(\theta)} \tag{4}$$

where Φ_n is the neutron fluence (1111.1 n cm^{-2} for all simulations), Ap is from Eq. (2), and N is the number of detected events. Efficiency is a unitless quantity; a value of 1 corresponds to perfect (100%) neutron detection efficiency. Fig. 17 plots the efficiency versus neutron energy E_n for the bare and Cd-wrapped sensors, for neutrons incident at an angle of 0°. Fig. 18 reports the energy- and angle-dependent response of the NSS sensors for a subset of incidence angles (θ = 0°, 15°, 30°, 45°, 60°, 75°, and 90°) to highlight the magnitude of the efficiency change as the neutron incidence angle changes. Angular sampling was achieved in the Geant4 simulation by rotating the sensor about its center and leaving the neutron beam geometry unchanged.

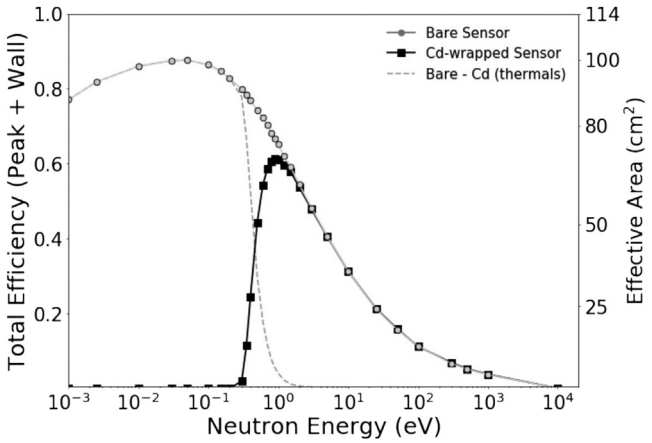

Fig. 17. Total neutron detection efficiency (ε) and effective area (A_{eff}) of the NSS sensors in the reference ($\theta = 0°$) geometry.

The neutron-energy and incidence-angle-dependent effective area of the sensors $A(E_{\mathrm{n}}, \theta)$ – defined as the equivalent area of a sensors with 100% neutron detection efficiency – is calculated as:

$$A\left(E_n, \theta\right) = \frac{N(E_n, \theta)}{\Phi_n} \tag{5}$$

and has units of cm^2.

At the peak efficiency values, >80,000 events were recorded in the sensors and the statistical uncertainty is <0.5%. At 1000 eV, the simulations generally returned ~4000 events in each sensor, corresponding to an uncertainty of ~1.5%. These values are small compared to the systematic uncertainties associated with the NSS and our simulations (see Table 5). Fig. 17 also plots the effective area versus neutron energy E_{n} for the bare and Cd-wrapped sensors, for neutrons incident at an angle of 0°.

The detection efficiency varies as a function of the pulse-height channel range used for analysis, due to gain loss near the dead region of the detector [12,13]. Detailed characterization of the Psyche Neutron Spectrometer (NS) ^{3}He sensors provided detailed characterization of this position-dependent efficiency loss near the ends of the active gas volume [7]. The efficiency loss was a manifestation of the neutron capture peak shifting to lower pulse height for neutron incidence close to the edge of the sensor. This problem is mitigated by using the total neutron efficiency values (Peak + Wall), as the loss of gas gain places Peak events in the Wall effect region and thus the gas-gain-efficiency loss is significantly reduced. Additionally, use of the Peak + Wall event efficiency and effective area results in a net increase in measured events throughout the sensor, not just near the end of the active area, as the Peak-to-wall-event ratio decreases significantly as neutron energy decreases.

5. Lessons for operation of NSS

Simplicity of design and operation, along with low resources, are the hallmarks of the NSS instrument. There are just two tunable operating parameters for NSS; the lower-level discriminator (threshold) and the high-voltage bias. The science calibration data reported here provides a basis for making informed recommendations for the best choice values for these parameters.

Our calibration and benchmarked simulations provide a strong basis for precise interpretation of NSS measurements. We have:

- A well-characterized understanding of the detector response (gain, efficiency) versus bias voltage,
- Laboratory measurements of the pulse-height range for gamma-ray and neutron signals,
- Experimental verification of the performance of the available thresholds,
- Accurate, benchmarked simulations of the detector response, including cross-calibration to a NIST-calibrated sensor, and
- Characterized systematic uncertainties of <6.3%.

Based on this information, we make some recommendations for the operation of the NSS on the lunar surface.

Bias voltages of 1500 V and above are available, in increments of 100 V. We recommend the use of 1600 V bias voltage, as the gain this provides (x17) is best matched to the intrinsic gain of the system (preamplifiers and electronics). The result is a peak position of channel ~24 (in the bare sensor) and ~23 (in the Cd sensor). In principle, 1500 V is also acceptable, which places the peaks around channel 14. Bias voltage values of 1700 V and higher place the neutron capture peak in the overload channel (channel 31), where it is indistinguishable from sources of background. Placement of the neutron capture peak in the overload channel would negate an intrinsic strength of neutron measurements with ^{3}He GPCs and compromise all reported measurements, thus we do not recommend the use of bias voltages of 1700+ V.

All of our laboratory data (e.g Figs. 5, 9) indicate that gamma-ray induced background are low for the spectral region that includes wall-effect and/or capture-peak neutrons (> channel 6). We have shown that lower-level discriminator (threshold) values of channel 3 are sufficient to remove the majority of the gamma-ray background and preserve the neutron signal in the laboratory environment. On the Moon, cosmic-ray proton interactions in the sensor add an additional background that has not been characterized. The ideal option is to preserve as much of the spectrum as possible for analysis on the ground, which argues for a

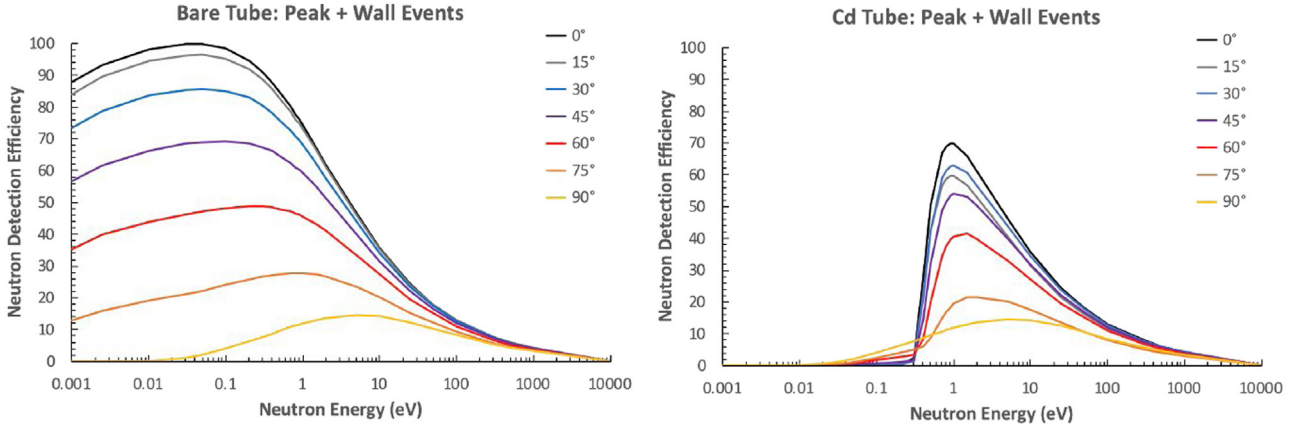

Fig. 18. Angle- and energy-dependent response of the bare (left) and Cd-covered (right) NSS sensors.

value of channel 0 or 1. This means that post-process of the spectrum is required to derive count rates. It may be as simple as a summing region of interest, or it may require background fitting and subtraction, depending on the range of the proton induced pulse heights.

In order to mitigate the unmeasured loss of efficiency due to the end-effect gain loss, count rates should be derived using the wall effect and neutron capture peak events. In this scenario, the simulated efficiencies values are highly accurate, having a systematic uncertainty of <6.3%. Any count rate summing should occur on gain-corrected summed spectra. However, TVAC data has shown that temperature-induced gain shifts are mild (~1 channel/95 °C for the bare sensor, (~2 channels/95 °C for the Cd-wrapped sensor). These values are for the NSS ETU-2 unit, and should be verified for other systems. Summing measurements acquired on the lunar surface as a function of temperature will provide the needed information. *

Declaration of competing interest

The authors declare the following financial interests/personal relationships which may be considered as potential competing interests: Patrick Peplowski reports financial support was provided by NASA.

Data availability

Data will be made available on request.

Acknowledgments

The Neutron Spectrometer System has been developed under funding from the National Aeronautics and Space Administration (NASA), USA. NASA provided funding to the Johns Hopkins Applied Physics Laboratory (JHU/APL), USA via contract 80MSFC20F0179. PNP thanks Spencer Disque and Mark Hoff (JHU/APL) for assistance designing and assembling the neutron pile, Zachary Yokley (JHU/APL) for assistance with the data acquisition system, and John Goldsten (JHU/APL) for helpful discussions during the calibration campaign that resulted in improvements to the neutron pile measurements. Finally, we thank David J. Lawrence and Luis Teodoro for providing a helpful review of this manuscript prior to submission.

References

[1] W.C. Feldman, S. Maurice, A.B. Binder, B.L. Barraclough, R.C. Elphic, D.J. Lawrence, Fluxes of fast and epithermal neutrons from Lunar prospector: Evidence for water ice at the Lunar poles, Science 281 (5382) (1998) 1496–1500.

[2] W.C. Feldman, W.V. Boynton, R.L. Tokar, T.H. Prettyman, O. Gasnault, S.W. Squyres, R.C. Elphic, D.J. Lawrence, S.L. Lawson, S. Maurice, G.W. McKinney, Global distribution of neutrons from Mars: Results from Mars Odyssey, Science 297 (5578) (2002) 75–78.

[3] I.G. Mitrofanov, M.L. Litvak, A.B. Varenikov, Y.N. Barmakov, A. Behar, Y.I. Bobrovnitsky, E.P. Bogolubov, W.V. Boynton, K. Harshman, E. Kan, A.S. Kozyrev, Dynamic Albedo of neutrons (DAN) experiment onboard NASA's Mars Science Laboratory, Space Sci. Rev. 170 (1) (2012) 559–582.

[4] R.E. Lingenfelter, E.H. Canfield, W.N. Hess, The Lunar neutron flux, J. Geophys. Res. 66 (9) (1961) 2665–2671.

[5] W.C. Feldman, R.C. Reedy, D.S. McKay, Lunar neutron leakage fluxes as a function of composition and hydrogen content, Geophys. Res. Lett. 18 (11) (1991) 2157–2160.

[6] R.C. Elphic, J.L. Heldmann, A. Colaprete, D.R. Hunt, M.C. Deans, D.S. Lim, G. Foil, T. Fong, the MVP Science, Data system and rover operations team, 2015, in: 46th Lunar and Planetary Science Conference, Abstract 2885, https://www.hou.usra.edu/meetings/lpsc2015/pdf/2885.pdf.

[7] P.N. Peplowski, Z.W. Yokley, M. Liebel, S. Cheng, R.C. Elphic, S.F. Hoogerheide, D.J. Lawrence, J.S. Nico, Position-dependent neutron detection efficiency loss in 3He gas proportional counters, Nucl. Instrum. Methods Phys. Res. A 982 (2020) 164574.

[8] W.C. Feldman, R.C. Byrd, B.L. Barraclough, J.E. Nordholt, H.O. Funsten, W.V. Boynton, S.H. Bailey, J. Moersch, Calibration of a space thermal/epithermal neutron detector: The Mars observer Gamma-ray spectrometer anticoincidence shield, Nucl. Instrum. Methods Phys. Res. A 362 (2–3) (1995) 561–573.

[9] J.W. Marsh, D.J. Thomas, M. Burke, High resolution measurements of neutron energy spectra from AmBe and AmB neutron sources, Nucl. Instrum. Methods Phys. Res. A 366 (2–3) (1995) 340–348.

[10] D.J. Lawrence, W.C. Feldman, R.C. Elphic, R.C. Little, T.H. Prettyman, S. Maurice, P.G. Lucey, A.B. Binder, Iron abundances on the lunar surface as measured by the Lunar Prospector gamma-ray and neutron spectrometers, J. Geophys. Res.: Planets 107 (E12) (2002) 13-1.

[11] R. Radev, T. McLean, Neutron Sources for Standard-Based Testing, Lawrence Livermore National Laboratory, 2014, LLNL-TR-664160, https://e-reports-ext.llnl.gov/pdf/785407.pdf.

[12] N. Takeda, K. Kudo, Neutron response functions improved by taking into consideration measured edge effect of 3He proportional counter, IEEE Trans. Nucl. Sci. 41 (4) (1994) 880–883.

[13] K. Kudo, N. Takeda, A. Uritani, S. Koshikawa, Y. Shibata, K. Kobayashi, T. Yoshimoto, Ideal response function of a 3He proportional counter to thermal neutrons determined by different length counters, Nucl. Instrum. Methods Phys. Res. B 213 (2004) 305–309.